

**NIA Report No. 2008-12**



# Accuracy of Gradient Reconstruction on Grids with High Aspect Ratio

*Boris Diskin*  
*National Institute of Aerospace, Hampton, Virginia*

*James Thomas*  
*Computational Aerosciences Branch, NASA Langley Research Center, Hampton Virginia*

# ACCURACY OF GRADIENT RECONSTRUCTION ON GRIDS WITH HIGH ASPECT RATIO

BORIS DISKIN\* AND JAMES L. THOMAS†

## Abstract.

Gradient approximation methods commonly used in unstructured-grid finite-volume schemes intended for solutions of high Reynolds number flow equations are studied comprehensively. The accuracy of gradients within cells and within faces is evaluated systematically for both node-centered and cell-centered formulations. Computational and analytical evaluations are made on a series of high-aspect-ratio grids with different primal elements, including quadrilateral, triangular, and mixed-element grids, with and without random perturbations to the mesh. Both rectangular and cylindrical geometries are considered; the latter serves to study the effects of geometric curvature. The study shows that the accuracy of gradient reconstruction on high-aspect-ratio grids is determined by a combination of the grid and the solution. The contributors to the error are identified and approaches to reduce errors are given, including the addition of higher-order terms in the direction of larger mesh spacing. A parameter  $\Gamma$  characterizing accuracy on curved high-aspect-ratio grids is discussed and an approximate-mapped-least-square method using a commonly-available distance function is presented; the method provides accurate gradient reconstruction on general grids. The study is intended to be a reference guide accompanying the construction of accurate and efficient methods for high Reynolds number applications.

**Key words.** unstructured grids, finite-volume discretizations, accuracy analysis

**AMS subject classifications.** 65N12, 76M12

**1. Introduction.** Finite volume discretization (FVD) schemes on unstructured grids with high aspect ratio are routinely encountered in computational fluid dynamics simulations of viscous flows at high Reynolds number. Many second-order FVD schemes require piecewise constant gradient reconstruction – within control volumes for inviscid fluxes and within control-volume boundaries (faces) for viscous fluxes. Gradients are also required for evaluation of source terms in turbulence equations. Accuracy of gradient reconstruction on unstructured grids has drawn research attention for a long time. Since 1970, the finite-element community studied the gradient reconstruction accuracy on triangles as a function of their angles [2, 4, 10, 14, 16]. A series of more recent studies [11, 12, 15] considered the gradient accuracy on curvilinear grids with high aspect ratio. While these publications addressed important aspects of the problem, a general understanding of the accuracy of various gradient approximations has not evolved. This paper reports on a comprehensive and systematic study of accuracy of gradients involved in FVD schemes on general two-dimensional (2D) grids with high aspect ratio.

The study is concerned with gradient reconstruction in the interior (no boundary effects considered) and shows that the accuracy is determined by a *combination* of grid and solution. On general non-symmetric meshes with aspect ratios sufficiently high that the product of the aspect ratio and the greater mesh spacing is much larger than one, any conventional gradient reconstruction method produces large errors for gradients of well-resolved and smooth solutions that vary predominantly in the direction of greater mesh spacing.

---

\*National Institute of Aerospace (NIA), 100 Exploration Way., Hampton, VA 23666-6147 (bdiskin@nianet.org).

†Computational Aerosciences Branch, NASA Langley Research Center, Mail Stop 128, Hampton, VA 23681-2199 (James.L.Thomas@nasa.gov).

Two geometries have been considered: rectangular and cylindrical. The cylindrical geometry is representative of grids with curvature-induced deformations. The paper studies unstructured grid methods applied to both regular and irregular grids. A grid is classified as regular if it has (1) a periodic node connectivity pattern (the number of edges per node changes periodically) and (2) a periodic cell pattern. Thus regular grids can be analyzed by Fourier analysis. Violation of either of these properties makes the grid irregular.

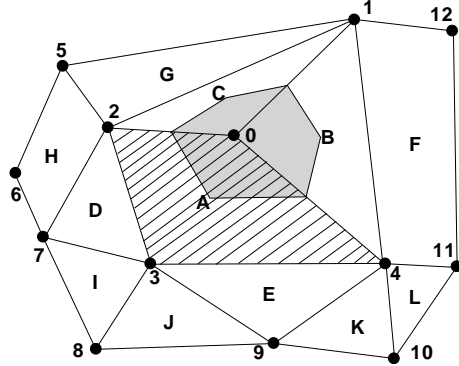


FIG. 1.1. Control-volume partitioning for finite-volume discretizations. Numbers 0 – 12 and letters A – L denote grid nodes and primal cell centers, respectively. The control volume for a node-centered discretization around the grid node 0 is shaded. The control volume for a cell-centered discretization around the cell center A is hashed.

Cell-centered and node-centered discretizations are considered. *Cell-centered discretizations* assume solutions are defined at the centers of the primal grid cells with the primal cells serving as the control volumes. The cell center coordinates are typically defined as the averages of the coordinates of the cell’s vertexes. *Node-centered discretizations* assume solutions are defined at the primal mesh nodes. For node-centered schemes, control volumes are constructed around the mesh nodes by the median-dual partition: the centers of primal cells are connected with the midpoints of the surrounding faces. These non-overlapping control volumes cover the entire computational domain and compose a mesh that is dual to the primal mesh. Both cell-centered and node-centered control-volume partitions are illustrated in Figure 1.1.

The material in this paper is presented in the following order. Section 2 describes the gradient approximation methods considered in this paper. Section 3 presents analysis and computations for high aspect ratio grids in a rectangular geometry. Specific difficulties related to curvature-induced grid deformation are analyzed in Section 4. Some discussions and conclusions are provided in Sections 5 and 6.

**2. Gradient Approximation Methods.** For both node-centered and cell-centered formulations, gradients can be classified as *within-cell gradients (C-gradients)* and *within-face gradients (F-gradients)*. The C-gradient, which is used for inviscid fluxes, is reconstructed within a control volume. Accuracy of the C-gradient is evaluated by comparing the reconstructed C-gradient,  $\nabla_r^c$ , with the exact gradient,  $\nabla_{\text{exact}}^c$ , computed at the control-volume center. The F-gradient, which is used for viscous fluxes, is reconstructed within a control-volume face. Accuracy of the F-gradient is evaluated by comparing the reconstructed F-gradient,  $\nabla_r^f$ , with the exact gradient,  $\nabla_{\text{exact}}^f$ , computed at the face center.

The accuracy of gradient reconstruction is measured as the relative gradient error. For example, relative error of the C-gradient is evaluated as

$$E_{\text{rel}} = \frac{\|\epsilon\|}{\|G\|}, \quad (2.1)$$

where functions  $\epsilon$  and  $G$  define point-wise amplitudes of the gradient error and the exact gradient, respectively,

$$\epsilon = |\nabla_r^c U^h - \nabla_{\text{exact}}^c U|, \quad \text{and} \quad G = |\nabla_{\text{exact}}^c U|; \quad (2.2)$$

$U$  and  $U^h$  are a differentiable test function and its discrete representation (usually injection) on a given grid, respectively;  $\|\cdot\|$  is a norm of interest computed over the entire computational domain. All estimates of the relative gradient reconstruction accuracy reported in the following sections are obtained in numerical computations. The estimates are supported by the Fourier analysis performed for several representative examples. For example, in a rectangular geometry, the analytical test function is  $e^{i(\alpha x + \beta y)}$ , and the gradient norm is evaluated as  $\sqrt{\alpha^2 + \beta^2}$ .

The majority of gradient reconstruction methods can be characterized as either element-free or element-based methods.

**2.1. Element-free gradient reconstruction.** The element-free approach typically relies on a least-square method. In this paper, four types of least-square methods are considered. In Cartesian coordinates, both weighted (WLSQ) and unweighted (ULSQ) least-square methods are considered. In the WLSQ method, the contributions to the minimized functional are weighted with weights inversely proportional to the distance from the central point; in the ULSQ method, all contributions are equally weighted. For the gradient approximation in regions with curvature, two least-square methods in a mapped domain are introduced: an exact mapping (EMLSQ) method and a more general approximate mapping (AMLSQ) method. C-gradient fits are denoted with a leading C designation, as CULSQ, CWLSQ, CEMLSQ, and CAMLSQ; F-gradient fits are denoted with a leading F designation, as FULSQ, FWLSQ, FEMLSQ, and FAMLSQ. The C-gradient fits recover the solution value at the control-volume center; two equations are solved (three in 3D). The F-gradient fits require solution of three equations (four in 3D).

The stencils used in the C-gradient fits are discussed with respect to Figure 1.1. For node-centered formulations, a typical stencil includes all nodes connected by an edge to the given node; for node 0, the stencil involves neighbors 1, 2, and 4. For cell-centered formulations, two types of stencils are considered — basic and augmented. The basic stencil involves only centers of face-neighbor cells and the augmented stencil includes the cells that share a vertex with the given cell. For cell-center  $A$ , the basic stencil includes neighbors  $B, C, D$ , and  $E$ ; the augmented stencil includes additionally neighbors  $F, G, H, I, J, K$ , and  $L$ .

For cell-centered formulations, the least-square stencils involved in F-gradient reconstruction include the centers of the two cells sharing the face and face neighbors of these two cells that share at least one vertex of the target face. With reference to Figure 1.1, the stencil for gradient reconstruction at face  $[\mathbf{r}_0, \mathbf{r}_4]$  involves neighbors  $A, B, C, E$ , and  $F$ . Here,  $\mathbf{r}_i$  is the coordinate vector of the node  $i$ . For gradient reconstruction at face  $[\mathbf{r}_3, \mathbf{r}_4]$ , the least-square stencil involves neighbors  $A, E, D, J, K$ , and  $B$ . Although applications of similar least-square methods for F-gradient reconstruction in node-centered formulations are entirely possible, these methods are applied only for cell-centered formulations in this paper.

Note that an element-free face gradient can be combined with a directional contribution across the face to determine the total F-gradient. Although not studied in this paper, an F-gradient can be approximated as an average of the C-gradients defined at the cells sharing the face,

For cell-centered formulations, another common method for F-gradient reconstruction is a node averaging (NA) method. It is closely related to the least-square methods; solution values are reconstructed at the nodes from the surrounding cell centers. With respect to Figure 1.1, the solution at the node 0 is reconstructed by averaging solutions defined at the cell centers  $A$ ,  $B$ , and  $C$ . The solution reconstruction proposed in [9, 13] and used in [6] is an averaging procedure that is based on a constrained optimization to satisfy some Laplacian properties. It has been shown in [7] that this averaging procedure is equivalent to an unweighted least-square linear fit. For F-gradient reconstructions, the derivative along the face is computed as the divided difference between the solution values reconstructed at the nodes. The gradient is resolved from the derivative along the face and the derivative along the edge connecting the cell centers across the face. For the face  $[\mathbf{r}_0, \mathbf{r}_4]$ , the face derivative is computed using solutions reconstructed by node averaging at the nodes 0 and 4; the edge derivative is computed using solutions at cell centers  $A$  and  $B$ .

**2.2. Element-based gradient reconstruction.** The element-based methods require solutions at the element faces and reconstruct gradients with the Green-Gauss (GG) formula

$$\nabla U = \frac{1}{\Omega} \oint_{\partial\Omega} U ds, \quad (2.3)$$

where  $\Omega$  is the element volume, integration is performed over the element boundary,  $\partial\Omega$ , and  $ds$  is the differential of the directed-area vector. The considered element can be either a primal element or a control-volume element; although, in this paper, the GG method is applied only over primal elements. For the second-order accuracy, the integral over each element face is approximated by the product of the solution computed at the face center and the directed area vector of the corresponding face. The directed area vector is defined as the outward normal vector with the amplitude equal to the face area.

For node-centered formulations, the GG method is used for F-gradient reconstruction. Solution values at the face-midpoints are obtained simply by averaging the nodal values. For cell-centered formulations, the GG method is applied for C-gradient reconstruction. The face-midpoint values are obtained either from F-gradient least-square computations or by averaging the nodal values obtained through the NA method. C-gradients computed in this manner are notated by the method used to obtain the face value plus GG.

Tables 2.1 and 2.2 summarize the methods studied in this paper for C- and F-gradient reconstruction, respectively, for node-centered and cell-centered formulations.

### 3. Gradient approximation in rectangular geometry.

**3.1. Grids.** The grids generated in the rectangular geometry are derived from an underlying Cartesian grid with meshsizes  $h_x$  and  $h_y$  and the aspect ratio  $A = \frac{h_x}{h_y} \gg 1$ ; both meshsizes of the underlying grids are assumed to be small,  $h_y \ll h_x \ll 1$ .

Six types of 2D grids are considered: (I) *regular quadrilateral (i.e., Cartesian) grids*; (II) *regular triangular grids* derived from the regular quadrilateral grids by

TABLE 2.1  
Methods for  $C$ -gradient reconstruction.

Formulation	Methods
Node centered	element-free methods: CULSQ, CWLSQ, CEMLSQ, CAMLSQ
Cell centered	element-free methods with basic and augmented stencils: CULSQ, CWLSQ, CEMLSQ, CAMLSQ; element-based methods: NA+GG, FULSQ+GG, FWLSQ+GG, FEMLSQ+GG, FAMLSQ+GG

TABLE 2.2  
Methods for  $F$ -gradient reconstruction.

Formulation	Methods
Node centered	element-based GG method
Cell centered	element-free methods: NA, FULSQ, FWLSQ, FEMLSQ, FAMLSQ

the same diagonal splitting of each quadrangle; (III) *random triangular grids*, in which regular quadrangles are split by randomly chosen diagonals, each diagonal orientation occurring with probability of half; (IV) *perturbed triangular grids*, which are random triangular grids, with grid nodes perturbed from their initial positions by independent random shifts in each dimension by a fraction of the local meshsize; (V) *perturbed quadrilateral grids*, which are quadrilateral grids with randomly perturbed grid nodes; and (VI) *perturbed mixed-element grids*, in which perturbed quadrangles are randomly split or not split by randomly chosen diagonals. Grids of types (III), (IV), and (VI) are irregular because there is no periodic connectivity pattern. Grids of types (IV)-(VI) are irregular because there is no periodic pattern for distribution of stencil distances from the stencil center.

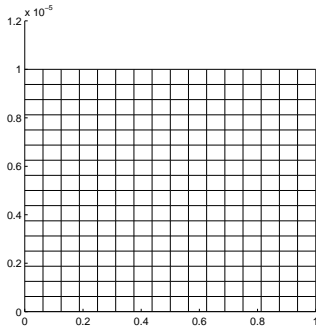
For most of the computational tests, the random node perturbation in each dimension is defined as  $\frac{1}{4}rh$ , where  $r \in [-1, 1]$  is a random number and  $h$  is the local meshsize along the given dimension. With these perturbations, triangular cells in the rectangular geometry are allowed to collapse, i.e., a cell may become a zero-volume cell, albeit with a probability of approaching zero. The random perturbations are introduced independently on all grids in grid refinement implying that grids (IV)-(VI) are grids with discontinuous metrics, e.g., ratios of neighboring cell volumes and face areas are random on all grids and do not approach unity in the limit of grid refinement.

The grid types are shown in Figure 3.1. For a better visualization of the grid topology, the grids are expanded in the  $y$ -direction.

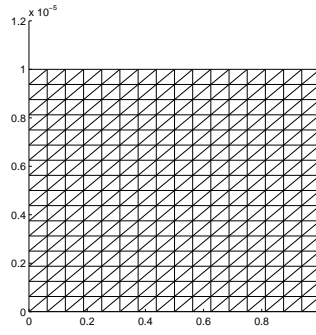
### 3.2. C-gradients.

**3.2.1. Node-centered schemes.** Node-centered least-square stencils on grids of type (I) and (II) are symmetric, and both CULSQ and CWLSQ methods provide second-order accurate gradient approximations. On more general grids the approximation accuracy deteriorates.

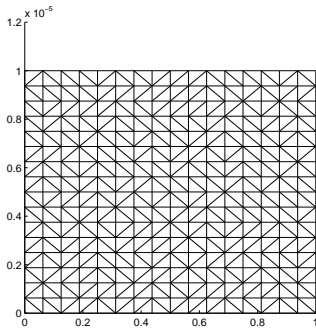
To illustrate this difficulty, let us consider a stencil on a random triangular grid of type (III) sketched in Figure 3.2. Assuming the center node at the origin, the coordinates of all stencil nodes are given in Table 3.1.



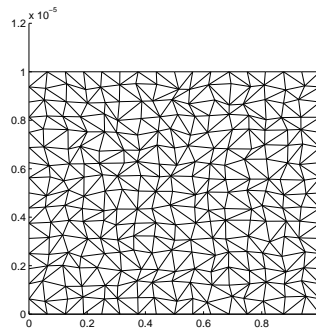
(a) Type (I): Regular quadrilateral grid



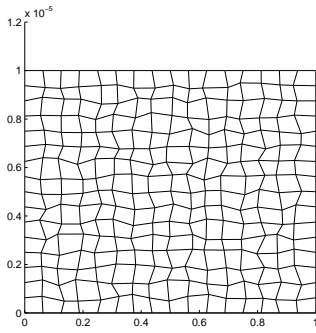
(b) Type (II): Regular triangular grid



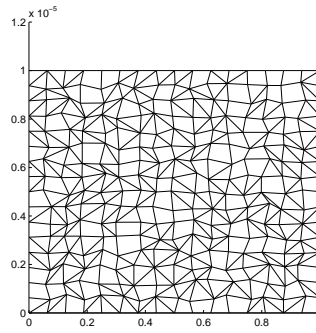
(c) Type (III): Random triangular grid



(d) Type (IV): Perturbed triangular grid



(e) Type (V): Perturbed quadrilateral grid



(f) Type (VI): Perturbed mixed grid

FIG. 3.1. Typical high-aspect-ratio rectangular grids expanded in the vertical direction.

The linear reconstruction  $f^r(x, y)$  of a general function  $f(x, y)$  is defined as

$$f^r \equiv f_0 + ax + by, \quad (3.1)$$

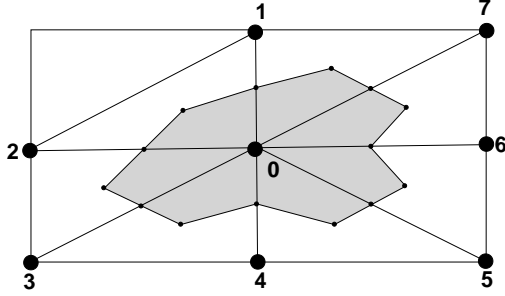


FIG. 3.2. Node-centered formulation: least-square stencil for the C-gradient of the shaded cell on a random triangular grid of type (III).

TABLE 3.1  
Coordinates of stencil points in Figure 3.2.

Point	$x$	$y$
0	0	0
1	0	$h_y$
2	$-h_x$	0
3	$-h_x$	$-h_y$
4	0	$-h_y$
5	$h_x$	$-h_y$
6	$h_x$	0
7	$h_x$	$h_y$

where  $f_0 = f(0, 0)$ . The components of the reconstructed gradient,  $\nabla_r^c f^r = (a, b)^T$ , are found by minimizing the sum of the squares of the (weighted) differences between the actual function and the linear fit computed at the stencil points.

$$\sum_{k=1}^7 [\mu_k (f_k^r - f_k)]^2 \rightarrow \min, \quad (3.2)$$

where  $\mu_k$  are weights

$$\begin{aligned} \mu_1 &= \mu_4 = \sqrt{1 + \nu_1^2}, \\ \mu_2 &= \mu_6 = \sqrt{1 + \nu_2^2}, \\ \mu_3 &= \mu_5 = \mu_7 = 1, \end{aligned} \quad (3.3)$$

and the subindex is a point indicator. For the CULSQ method,  $\nu_1 = \nu_2 = 0$ ; for the CWLSQ method,  $\nu_1 = \frac{1}{\nu_2} = A = \frac{h_x}{h_y}$ .

The result of minimization is

$$\begin{pmatrix} a \\ b \end{pmatrix} = \frac{1}{(5 + 2\nu_1^2)(5 + 2\nu_2^2) - 1} \begin{pmatrix} \frac{5 + 2\nu_1^2}{h_x} & -\frac{1}{h_{x_2}} \\ -\frac{1}{h_y} & \frac{5 + 2\nu_2^2}{h_y} \end{pmatrix} \mathbf{f}^{\mathbf{h}}, \quad (3.4)$$

where  $\mathbf{f}^{\mathbf{h}}$  is

$$\mathbf{f}^{\mathbf{h}} = \begin{pmatrix} -f_0 - f_2 - f_3 + f_5 + f_6 + f_7 + \nu_2^2(-f_2 + f_6) \\ f_0 + f_1 - f_3 - f_4 - f_5 + f_7 + \nu_1^2(f_1 - f_4) \end{pmatrix}. \quad (3.5)$$

Assuming  $h_y \ll h_x \ll 1$ , for the test function  $f = e^{i(\alpha x + \beta y)}$ , the leading terms in the gradient approximation are

$$\begin{aligned} a &\approx i\alpha - \frac{1}{h_x} \frac{3 + \nu_1^2}{(5 + 2\nu_1^2)(5 + 2\nu_2^2) - 1} (\alpha^2 h_x^2 - 2\alpha\beta h_x h_y + \beta^2 h_y^2), \\ b &\approx i\beta + \frac{1}{h_y} \frac{3 + \nu_2^2}{(5 + 2\nu_1^2)(5 + 2\nu_2^2) - 1} (\alpha^2 h_x^2 - 2\alpha\beta h_x h_y + \beta^2 h_y^2). \end{aligned} \quad (3.6)$$

In the case of solutions that are equally well-resolved in both directions, i.e.,  $\alpha h_x \approx \beta h_y \ll 1$ , which is a typical case for velocity components in viscous boundary layers, the relative error is small. For the CULSQ method and comparable frequencies  $\alpha \approx \beta$  (typical of pressure in viscous boundary layers),

$$\begin{aligned} a &\approx i\alpha - \frac{1}{8}\alpha^2 h_x, \\ b &\approx i\beta + \frac{1}{8}\alpha^2 \frac{h_x}{h_y}, \end{aligned} \quad (3.7)$$

and the relative gradient error is dominated by the error in the  $y$ -direction as

$$E_{\text{rel}} \approx \frac{1}{8} \frac{\alpha^2}{\sqrt{\alpha^2 + \beta^2}} A h_x. \quad (3.8)$$

The error is converging with first order in grid refinement ( $h_x \rightarrow 0$ ), but can be large for a grid/solution combination with  $\frac{\alpha^2}{\sqrt{\alpha^2 + \beta^2}} A h_x \gg 1$ .

For the CWLSQ method and comparable frequencies  $\alpha \approx \beta$ ,

$$\begin{aligned} a &\approx i\alpha - \frac{1}{10}\alpha^2 h_x, \\ b &\approx i\beta + \frac{3}{10}\alpha^2 h_y. \end{aligned} \quad (3.9)$$

and the relative error is small as long as  $\alpha^2 h_x \ll 1$ .

In general, the CWLSQ method helps to improve gradient reconstruction accuracy, if the least-square stencil includes points that are much closer to the center than others or, more specifically, if the largest ratio of distances to the center is comparable with the grid aspect ratio. This requirement is satisfied for unperturbed grids of types (I)-(III). Unfortunately, general grids with perturbed nodes (types (IV)-(VI)) produce stencils with points that are similarly distant from the control-volume center, i.e., the distance variation is not that large. The CWLSQ method does not guarantee a small relative error on such grids. Figure 3.3 illustrates convergence of the gradient approximation provided by the CULSQ and CWLSQ methods on perturbed triangular grids of type (IV). The computations are performed on grids with  $A = 10^6$  for the test function  $f = \sin(\frac{\pi}{50}x + \frac{\pi}{6})$ . The gradient error converges with the first order for both CULSQ and CWLSQ methods. On any given grid, the accuracy of the CWLSQ method is about an order of magnitude better than the accuracy of the CULSQ method. However, on grids with  $A h_x \gg 1$ , the relative gradient error of both methods is much greater than one.

Table 3.4 before Section 3.2.3 summarizes the performance of the node-centered CULSQ and CWLSQ methods on the tested grids. Appearance of the aspect ratio

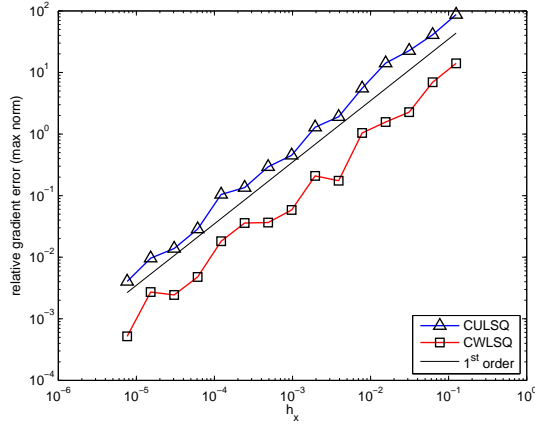


FIG. 3.3. Gradient approximation on randomly perturbed triangular grids of type (IV) with aspect ratio  $A = 10^6$ .

parameter,  $A$ , in the accuracy estimate indicates that the relative gradient error may be large for certain grid/solution combinations.

A general way to improve gradient accuracy is to amend the least-square fit function by including higher order terms in the directions of large meshsize, e.g.,

$$f^r \equiv f_0 + ax + by + cx^2; \quad (3.10)$$

the leading relative error term then becomes  $O(\alpha^3 Ah_x^2)$ . Additional high-order terms further reduce the relative error; the leading term becomes  $O(\alpha A(\alpha h_x)^p)$ , where  $p$  is the highest power of  $x$  in the fit function. The relative gradient error is guaranteed to be uniformly small, if the directional errors are comparable, i.e.,  $(\alpha h_x)^{p+1} \approx \beta^2 h_y^2$ .

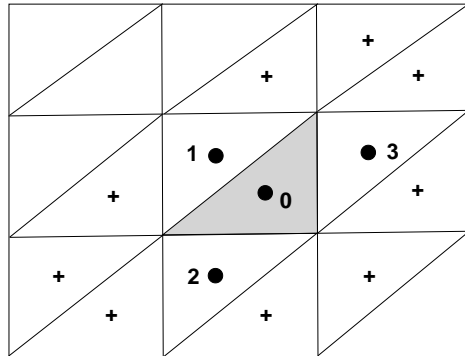


FIG. 3.4. Cell-centered formulation: least-square stencil for the C-gradient of the shaded cell on a regular triangular grid of type (II). Black dots denote the basic stencil; crosses denote additional cells contributing to the augmented stencil.

TABLE 3.2  
Coordinates of basic stencil points in Figure 3.4.

Point	$x$	$y$
0	0	0
1	$-h_x/3$	$h_y/3$
2	$-h_x/3$	$-2h_y/3$
3	$2h_x/3$	$h_y/3$

**3.2.2. Cell-centered schemes.** For cell-centered formulations, both CULSQ and CWLSQ methods provide small relative gradient error on regular grids of types (I) and (II) for basic and augmented stencils, even though the stencils on grids of type (II) are not symmetric. To show this, let us consider a basic stencil for the shaded cell shown in Figure 3.4. With the origin at the cell center, the coordinates of the stencil vertexes are given in Table 3.2. The linear fit is the same as in (3.1). The components of the reconstructed gradient,  $\nabla_r^c f^r = (a, b)^T$ , are found by minimizing the functional

$$\sum_{k=1}^3 [\mu_k (f_k^r - f_k)]^2 \rightarrow \min, \quad (3.11)$$

For the CULSQ method,  $\mu_1 = \mu_2 = \mu_3 = 1$ . For the CWLSQ method,  $\mu_1^2 = 1 + A^2$ ;  $\mu_2^2 = 4 + A^2$ ;  $\mu_3^2 = 1 + 4A^2$ .

The result of minimization is

$$\begin{pmatrix} a \\ b \end{pmatrix} = \frac{3}{(\mu_1^2 + 4\mu_2^2 + \mu_3^2)(\mu_1^2 + \mu_2^2 + 4\mu_3^2) - (-\mu_1^2 + 2\mu_2^2 + 2\mu_3^2)^2} \begin{pmatrix} \frac{\mu_1^2 + 4\mu_2^2 + \mu_3^2}{h_x} & \frac{\mu_1^2 - 2\mu_2^2 - 2\mu_3^2}{h_x} \\ \frac{\mu_1^2 - 2\mu_2^2 - 2\mu_3^2}{h_y} & \frac{\mu_1^2 + \mu_2^2 + 4\mu_3^2}{h_y} \end{pmatrix} \mathbf{f}^h,$$

where

$$\mathbf{f}^h = \begin{pmatrix} -\mu_1^2(f_1 - f_0) - \mu_2^2(f_2 - f_0) + 2\mu_3^2(f_3 - f_0) \\ \mu_1^2(f_1 - f_0) - 2\mu_2^2(f_2 - f_0) + \mu_3^2(f_3 - f_0) \end{pmatrix}.$$

For the test function  $f = e^{i(\alpha x + \beta y)}$ , the reconstructed gradient components are estimated as

$$\begin{aligned} a &\approx i\alpha - \frac{3}{2h_x} \frac{\alpha^2 h_x^2 (-\mu_1^2 \mu_2^2 + \mu_1^2 \mu_3^2 + 3\mu_2^2 \mu_3^2) + \alpha \beta h_x h_y 2\mu_3^2 (\mu_1^2 + 2\mu_2^2) + \beta^2 h_y^2 2\mu_2^2 (\mu_3^2 - \mu_1^2)}{(\mu_1^2 + 4\mu_2^2 + \mu_3^2)(\mu_1^2 + \mu_2^2 + 4\mu_3^2) + (\mu_1^2 - 2\mu_2^2 - 2\mu_3^2)^2}, \\ b &\approx i\beta - \frac{3}{2h_y} \frac{\alpha^2 h_x^2 2\mu_3^2 (\mu_1^2 - \mu_2^2) - \alpha \beta h_x h_y \mu_2^2 (\mu_1^2 + 2\mu_3^2) + \beta^2 h_y^2 (-\mu_1^2 \mu_2^2 + \mu_1^2 \mu_3^2 - 3\mu_2^2 \mu_3^2)}{(\mu_1^2 + 4\mu_2^2 + \mu_3^2)(\mu_1^2 + \mu_2^2 + 4\mu_3^2) + (\mu_1^2 - 2\mu_2^2 - 2\mu_3^2)^2}. \end{aligned} \quad (3.12)$$

In general, for comparable  $\alpha$  and  $\beta$ , the error term corresponding to  $\alpha^2$  in the estimate for the  $y$ -directional gradient component,  $b$ , is proportional to  $\frac{h_x^2}{h_y}$  and may become large on grids with  $Ah_x \gg 1$ . However, for this specific case, the coefficient

$$\frac{h_x^2}{h_y} \frac{2\mu_3^2 (\mu_1^2 - \mu_2^2)}{(\mu_1^2 + 4\mu_2^2 + \mu_3^2)(\mu_1^2 + \mu_2^2 + 4\mu_3^2) + (\mu_1^2 - 2\mu_2^2 - 2\mu_3^2)^2}$$

becomes vanishingly small for both the CULSQ and CWLSQ reconstruction methods.

The error cancellations observed on grids of type (II) do not occur on more general grids. For example, on grids of type (III), accuracy of the CULSQ method

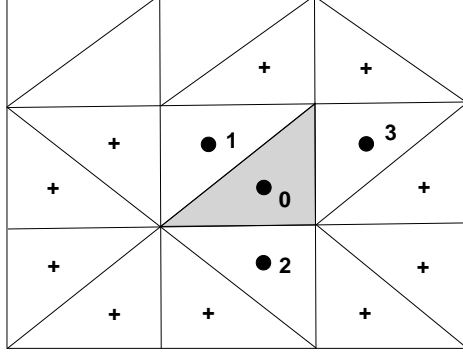


FIG. 3.5. Cell-centered formulation: least-square stencil for the C-gradient on a random triangular grid of type (III), for which the CULSQ methods generates a large relative error.

TABLE 3.3  
Coordinates of basic stencil points in Figure 3.5.

Point	$x$	$y$
0	0	0
1	$-h_x/3$	$h_y/3$
2	0	$-2h_y/3$
3	$2h_x/3$	$h_y/3$

deteriorates; typical basic and augmented stencils are illustrated in Figure 3.5. The coordinates of the basic stencil are given in Table 3.3.

Minimization problem (3.11) is solved with  $\mu_1 = \mu_2 = \mu_3 = 1$  for the CULSQ method and with  $\mu_1^2 = \frac{1}{1+A^2}$ ;  $\mu_2^2 = \frac{1}{4}$ ;  $\mu_3^2 = \frac{1}{1+4A^2}$  for the CWLSQ method. The solution is given by

$$\begin{pmatrix} a \\ b \end{pmatrix} = \frac{3}{(\mu_1^2 + 4\mu_2^2 + \mu_3^2)(\mu_1^2 + 4\mu_3^2) - (\mu_1^2 - 2\mu_3^2)^2} \begin{pmatrix} \frac{\mu_1^2 + 4\mu_2^2 + \mu_3^2}{h_x} & \frac{\mu_1^2 - 2\mu_3^2}{h_x} \\ \frac{\mu_1^2 - 2\mu_3^2}{h_y} & \frac{\mu_1^2 + 4\mu_3^2}{h_y} \end{pmatrix} \mathbf{f}^{\mathbf{h}},$$

where

$$\mathbf{f}^{\mathbf{h}} = \begin{pmatrix} -(-\mu_1^2 + 2\mu_3^2)f_0 - \mu_1^2 f_1 + 2\mu_3^2 f_3 \\ -(\mu_1^2 - 2\mu_2^2 + \mu_3^2)f_0 + \mu_1^2 f_1 - 2\mu_2^2 f_2 + \mu_3^2 f_3 \end{pmatrix}.$$

The test function  $f = e^{i(\alpha x + \beta y)}$  is again considered. For the CULSQ method with the basic stencil,

$$\begin{aligned} a &\approx i\alpha - \frac{1}{174} \frac{1}{h_x} (37\alpha^2 h_x^2 + 58\alpha\beta h_x h_y + 12\beta^2 h_y^2), \\ b &\approx i\beta - \frac{1}{174} \frac{1}{h_y} (18\alpha^2 h_x^2 - 31\beta^2 h_y^2), \end{aligned} \quad (3.13)$$

and, for comparable  $\alpha$  and  $\beta$ , the relative gradient error is proportional to the grid aspect ratio,  $A$ ,

$$E_{\text{rel}} \approx \frac{3}{29} \frac{\alpha^2}{\sqrt{\alpha^2 + \beta^2}} A h_x; \quad (3.14)$$

it may become large, if  $Ah_x \gg 1$ . For the augmented stencil, the CULSQ relative gradient error remains proportional to the grid aspect ratio.

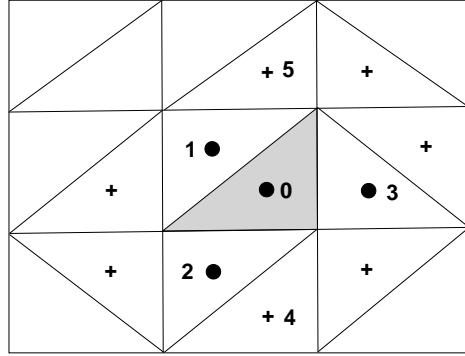


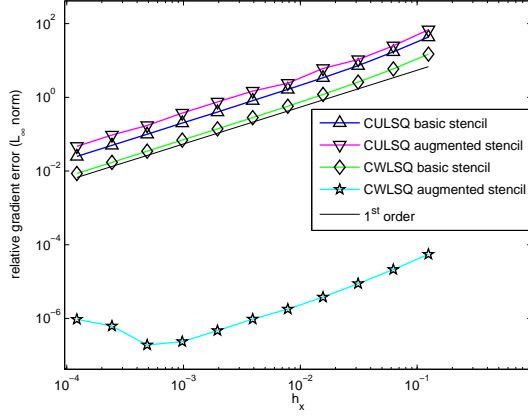
FIG. 3.6. *Triangular grid for which the CWLSQ method generates a large relative error with basic stencil.*

Accuracy provided by CWLSQ method depends on the stencil configuration. For the basic stencil shown in Figure 3.5, the largest ratio of distances from the center is  $O(A)$ , and the CWLSQ method provides small relative gradient errors independent of grid aspect ratios. However, for another geometry shown in Figure 3.6, the largest distance ratio is less than two. Consequently, the accuracy of the CWLSQ method with the basic stencil is still proportional to  $A$ . The augmented stencil always includes points much closer to the center than other points. For example, the distances from the center to points 4 and 5 are much shorter than the distances to points 1, 2, and 3 for  $A \gg 1$ . The ratio of the distances becomes  $O(A)$ , and the CWLSQ method provides small relative gradient errors.

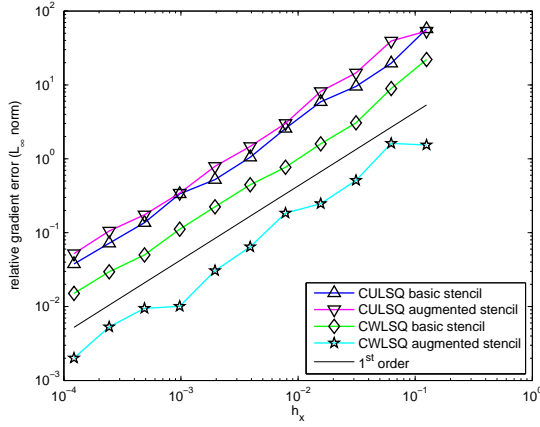
On general perturbed high-aspect ratio grids of types (IV)-(VI), both the CULSQ and CWLSQ methods generate large relative gradient errors. Figure 3.7 illustrates convergence of the  $L_\infty$ -norm of the errors on random triangular grids of types (III) and (IV). The test function,  $f = \sin(\frac{\pi}{50}x + \frac{\pi}{6})$ , varies smoothly in the direction of large meshsize,  $h_x$ , and the grid aspect ratio is fixed in grid refinement as  $A = 10^6$ . The results confirm predictions of the analysis. On grids of type (III), only the combination of the CWLSQ method with the augmented stencil provides accurate gradient reconstruction on all grids. On grids of type (IV) with  $Ah_x \gg 1$ , all methods produce large relative gradient errors. Element-based reconstruction methods, NA+GG, FULSQ+GG, and FWLSQ+G, do not provide accuracy benefits. Table 3.5 summarizes results reported in this section.

TABLE 3.4  
*Node-centered formulation: accuracy of C-gradient reconstruction.*

Grids	(I) and (II)	(III)	(IV)-(VI)
CULSQ	$O(h_x^2)$	$O(Ah_x)$	$O(Ah_x)$
CWLSQ	$O(h_x^2)$	$O(h_x)$	$O(Ah_x)$



(a) Random triangular grid of type (III)



(b) Randomly perturbed triangular grid of type (IV)

FIG. 3.7. Convergence of relative gradient errors in  $C$ -gradient reconstruction on random triangular grids for cell-centered formulation

**3.2.3. Summary on  $C$ -gradient approximation.** For second-order accuracy of inviscid fluxes, the asymptotic order of the reconstructed  $C$ -gradient is required to be at least first order. All the schemes considered in this section satisfy this requirement. The distinctions occur for certain combinations of solutions and cell/stencil geometries, for which the relative error is proportional to the grid aspect ratio as  $O(Ah_x)$  and may become large. For general high-aspect-ratio grids, the accuracy degradation occurs for solutions that vary predominantly in the direction of large mesh spacing.

Comparing Tables 3.4 and 3.5, the following conclusions about accuracy of  $C$ -gradients can be reached. For regular grids of types (I) and (II), both cell-centered

TABLE 3.5  
*Cell-centered formulation: accuracy of C-gradient reconstruction.*

Grids	(I)	(II)	(III)	(IV)–(VI)
CULSQ, basic stencil	$O(h_x^2)$	$O(h_x)$	$O(Ah_x)$	$O(Ah_x)$
CULSQ, augmented stencil	$O(h_x^2)$	$O(h_x)$	$O(Ah_x)$	$O(Ah_x)$
CWLSQ, basic stencil	$O(h_x^2)$	$O(h_x)$	$O(Ah_x)$	$O(Ah_x)$
CWLSQ, augmented stencil	$O(h_x^2)$	$O(h_x)$	$O(h_x)$	$O(Ah_x)$
NA+GG	$O(h_x^2)$	$O(h_x)$	$O(Ah_x)$	$O(Ah_x)$
FULSQ+GG	$O(h_x^2)$	$O(h_x)$	$O(Ah_x)$	$O(Ah_x)$
FWLSQ+GG	$O(h_x^2)$	$O(h_x)$	$O(Ah_x)$	$O(Ah_x)$

and node-centered formulations provide accurate gradients. For grids of type (III), which are typical for high-Reynolds turbulent-flow applications, each formulation has a preferable method, providing accurate gradient reconstruction on all grids independent of  $A$  – the CWLSQ method for node-centered formulations and the CWLSQ method with the augmented stencil for cell-centered formulations. For perturbed grids of types (IV)–(VI), both formulations suffer gradient accuracy degradation.

In those instances where degradation occurs, the leading component of the relative gradient error is proportional to  $O(|f_{xx}|Ah_x)$ , where  $f(x, y)$  is a test function. The magnitude of  $|f_{xx}|Ah_x$  can be estimated a posteriori for each control volume in order to determine if the computed gradient is accurate. Also, one can selectively add higher order terms (only those varying in the directions of large mesh spacing) to the least square fit to improve gradient reconstruction accuracy. The sufficient maximal power,  $p$ , of added terms can be determined from the condition  $|\partial_x^{(p+1)} f|Ah_x^p = O(1)$ .

### 3.3. F-gradient.

**3.3.1. Node-centered scheme.** For the F-gradient reconstruction with node-centered formulations, the GG method is used to reconstruct gradients at the primal cells. On fully triangular grids, integration over the median-dual boundary results in a formulation equivalent to a Galerkin finite-element scheme with a linear basis function [1, 3]. Mixed-element node-centered schemes also employ easily available edge derivatives to increase  $h$ -ellipticity of the discretization with no loss of accuracy [8].

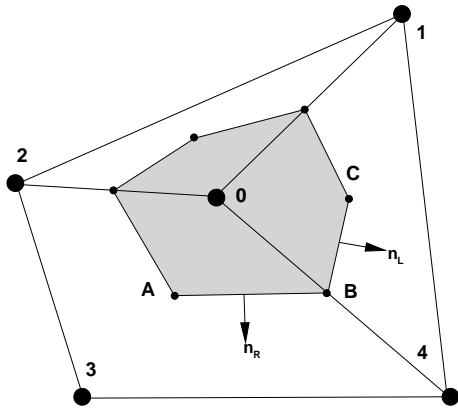


FIG. 3.8. *Illustration of F-gradient reconstruction on mixed grids for node-centered formulations.*

For illustration, let us consider a discretization on the mixed-element grid shown in Figure 3.8. The Green-Gauss formula,

$$\int_{\Omega} \nabla U d\Omega = \oint_{\partial\Omega} U ds, \quad (3.15)$$

is applied over a primal element,  $\Omega$ . It is known that on general (non-triangular) cells, the Green-Gauss formula does not recover a linear function [5], but still produces at least first-order accurate gradients.

The gradient,  $\nabla U_{BC}$ , at the dual face  $[B, C]$  is determined at the triangle  $\Delta_{014}$  as

$$\nabla U_{BC} = \overline{\nabla U}_{014} = \frac{1}{\Omega_{014}} \left( \frac{U_0 + U_4}{2} \mathbf{a}_{04} + \frac{U_4 + U_1}{2} \mathbf{a}_{41} + \frac{U_1 + U_0}{2} \mathbf{a}_{10} \right), \quad (3.16)$$

where the overbar denotes the Green-Gauss gradient evaluated on the primal cell identified by the point subscripts,  $U_i$  is the solution defined at the node  $i$ , and  $\mathbf{a}_{ij}$  denotes the face directed-area vector that is an outward normal vector with the amplitude equal to the area (length) of the corresponding edge linking the nodes  $i$  and  $j$ . Note, for this triangular element, the Green-Gauss method recovers the edge derivative,

$$\frac{U_4 - U_0}{|\mathbf{r}_4 - \mathbf{r}_0|} = \nabla U_{BC} \cdot \mathbf{e}_{04}, \quad (3.17)$$

where  $\mathbf{r}_i$  is the coordinate vector of the node  $i$  and

$$\mathbf{e}_{04} = \frac{\mathbf{r}_4 - \mathbf{r}_0}{|\mathbf{r}_4 - \mathbf{r}_0|} \quad (3.18)$$

is the unit vector aligned with the edge connecting nodes 0 and 4.

For the dual face  $[A, B]$ , the gradient,  $\nabla U_{AB}$ , is evaluated by the combination of the Green-Gauss method and the edge derivative as

$$\nabla U_{AB} = \overline{\nabla U}_{0234} + \left[ \frac{U_4 - U_0}{|\mathbf{r}_4 - \mathbf{r}_0|} - \overline{\nabla U}_{0234} \cdot \mathbf{e}_{04} \right] \mathbf{e}_{04}. \quad (3.19)$$

Note that for grids with dual faces perpendicular to edges, the edge gradient,  $\frac{U_4 - U_0}{|\mathbf{r}_4 - \mathbf{r}_0|} \mathbf{e}_{04}$ , is the only contributor to the normal gradient.

The combined F-gradient over the face  $ABC$  is computed at the point  $B$  as

$$\nabla_r^f U = \frac{(\nabla U_{AB} \cdot \mathbf{n}_R) + (\nabla U_{BC} \cdot \mathbf{n}_L)}{|\mathbf{n}_R + \mathbf{n}_L|}, \quad (3.20)$$

where  $\mathbf{n}_R$  and  $\mathbf{n}_L$  are directed areas of segments  $[A, B]$  and  $[B, C]$ , respectively.

The following classical example [2, 16] illustrates the difficulties of F-gradient reconstruction on grids with high aspect ratio. Consider a primal cell in the shape of an isosceles obtuse triangle, shown in Figure 3.9, with vertex coordinates given in Table 3.6.

For a general function  $f = f(x, y)$ , any method that precisely recovers the gradient of a linear function on a three-point stencil provides the following approximation to the gradient.

$$\nabla f \approx \left( \begin{array}{c} \frac{f_3 - f_1}{2h_x} \\ -\frac{f_3 - 2f_2 + f_1}{2h_y} \end{array} \right). \quad (3.21)$$

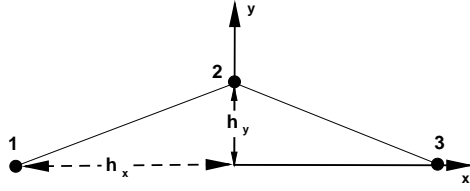


FIG. 3.9. *Obtuse triangle stencil.*

TABLE 3.6

*Vertex coordinates for the isosceles obtuse triangle shown in Figure 3.9.*

Point	$x$	$y$
1	$-h_x$	0
2	0	$h_y$
3	$h_x$	0

Performing the Taylor expansion at  $(x, y) = (0, 0)$  and assuming  $h_y \ll h_x \ll 1$  for the test function  $f = e^{i(\alpha x + \beta y)}$  with comparable frequencies  $\alpha \approx \beta$ , the leading terms in the gradient approximation are

$$\nabla f \approx \begin{pmatrix} i\alpha - i\frac{1}{6}\alpha^3 h_x^2 \\ i\beta + \frac{1}{2}\alpha^2 \frac{h_x^2}{h_y} \end{pmatrix}. \quad (3.22)$$

The relative error in gradient approximation,  $O\left(\frac{\alpha^2 A h_x}{\sqrt{\alpha^2 + \beta^2}}\right)$ , is again proportional to the grid aspect ratio,  $A = \frac{h_x}{h_y}$ , and can be large on grids with  $A h_x \gg 1$ .

Note that large relative errors in the gradient approximation are generated only on cells with an obtuse angle approaching  $180^\circ$ ; such cells occur on grids of types (IV)-(VI). The relative errors are small on triangles with two angles approaching  $90^\circ$ , such as those in grids of types (II) and (III). The F-gradient reconstruction accuracy is summarized in Table 3.7

**3.3.2. Cell-centered schemes.** For F-gradient reconstruction in cell-centered formulations, three methods are considered: the NA method [6, 9, 13] and two face-based least-square (FULSQ and FWLSQ) methods. Table 3.8 summarizes results from a series of numerical tests performed to study the accuracy of cell-centered F-gradient reconstruction. The test function is  $U = \sin\left(\frac{\pi}{50}x + \frac{\pi}{6}\right)$  and varies smoothly in the  $x$ -direction only. The aspect ratio  $A = 10^6$  is fixed in grid refinement. On grids of type (I), NA, FULSQ and FWLSQ methods are second-order accurate. On other grids, the methods demonstrate convergence with a first-order slope, but the magnitude of the relative errors is large on grids with  $A h_x \gg 1$ . The FWLSQ method

provides similar results to the FULSQ method for grid types (II) and (III) because the ratios of distances from the center in the stencils are  $O(1)$ .

TABLE 3.7  
*Node-centered formulations: accuracy of F-gradient reconstruction*

Grids	(I)	(II)	(III)	(IV) –(VI)
Green Gauss	$O(h_x^2)$	$O(h_x^2)$	$O(h_x)$	$O(Ah_x)$

TABLE 3.8  
*Cell-centered formulations: accuracy of F-gradient reconstruction*

Grids	(I)	(II)	(III)	(IV) –(VI)
NA	$O(h_x^2)$	$O(Ah_x^2)$	$O(Ah_x)$	$O(Ah_x)$
FULSQ	$O(h_x^2)$	$O(Ah_x^2)$	$O(Ah_x)$	$O(Ah_x)$
FWLSQ	$O(h_x^2)$	$O(Ah_x^2)$	$O(Ah_x)$	$O(Ah_x)$

As noted previously, weighted least-square methods are beneficial when the ratio of distances from the stencil center becomes  $O(A)$ , and the close points are displaced predominantly in the direction of small mesh spacing. A single such point is required for the CWLSQ method. The FWLSQ method require two such points to provide accuracy.

On highly irregular grids, the presence of only one close point (much closer to the stencil center than the other points) causes (rare) local sharp jumps in F-gradient error, generally observable only on large grids and in the  $L_\infty$  norm. In spite of the jumps, the error upper bound still converges with first order in grid refinement. For illustration purposes, Figure 3.10 shows convergence of the  $L_\infty$ -norm of relative gradient errors observed on randomly perturbed triangular grids of type (IV). In this test, the random mesh perturbations have been introduced by shifting each node in the Cartesian directions by  $\frac{3}{16}rh$ , where  $r \in [-1, 1]$  is a random number and  $h$  is either  $h_x$  or  $h_y$  for horizontal and vertical perturbations, respectively. The smaller perturbations (the random shift coefficient is  $\frac{3}{16}$  instead of  $\frac{1}{4}$  used in other computations) are used to avoid cell (near) collapses that may lead to infinite weights in the FWLSQ method.

**3.3.3. Summary on F-gradient approximation.** For second-order accuracy of viscous fluxes, the asymptotic order of reconstructed F-gradients is required to be at least first order. The schemes considered in this section satisfy this requirement. Similar to the C-gradient evaluation, a gradient accuracy degradation occurs for combinations of grids/stencils with  $Ah_x \gg 1$  and solutions that vary predominantly in the direction of large mesh spacing.

Comparing Tables 3.7 and 3.8, the following conclusions are drawn. For quadrilateral grids of types (I), both node-centered and cell-centered formulations provide accurate gradients. For unperturbed grids of types (II) and (III), the asymptotic order is second and first order, respectively, for both formulations. However, node-centered formulations possess an advantage over cell-centered formulations; the former always provides accurate approximations, while the accuracy of the latter may degrade to  $O(Ah_x)$ . In cell-centered formulations, the FWLSQ method does not provide any significant benefits over the FULSQ method. For perturbed grids of types (IV)-(VI) and for both formulations, the relative error in the gradient reconstruction is proportional to the grid aspect ratio.

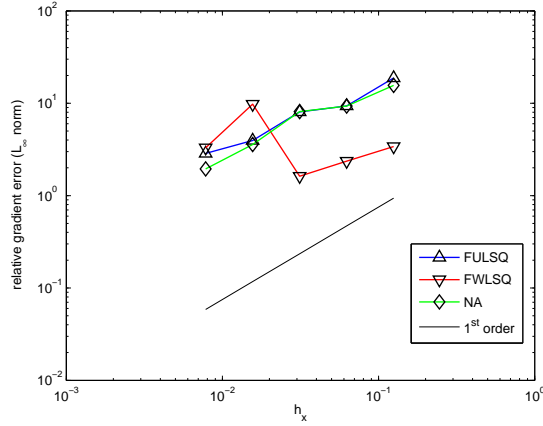


FIG. 3.10. Cell-centered formulation: relative gradient error of  $F$ -gradient reconstruction on perturbed grids of type (IV)

As discussed previously, accuracy of the reconstruction can be evaluated a posteriori. Accuracy of least-square methods can be improved by expanding the fit with additional higher-order terms varying in the direction of large mesh spacing; the gradient reconstruction for these functions is accurate on grids with small deformations ( $\Gamma \ll 1$ ).

#### 4. Gradient approximation in curved (cylindrical) geometry.

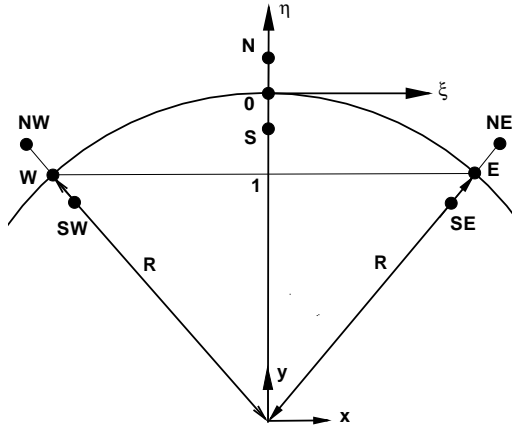


FIG. 4.1. Schematic of nodes near curved surface.

**4.1. Grids.** In cylindrical geometry, the grid nodes are generated from a polar-coordinate mapping,  $(r, \theta)$ , with spacings of  $h_r$  and  $h_\theta$ , respectively. The mesh is composed of grid nodes connected by straight-line segments. The grid aspect ratio is defined as the ratio of meshsizes in the angular (circumferential) and the radial directions,  $A = R \frac{h_\theta}{h_r}$ , where  $R$  is a characteristic radius of the computational domain.

The mesh deformation is characterized by a parameter  $\Gamma$ :

$$\Gamma = \frac{|\mathbf{r}_1 - \mathbf{r}_0|}{|\mathbf{r}_N - \mathbf{r}_0|} = \frac{R - R \cos(h_\theta)}{h_r} \approx \frac{Rh_\theta^2}{2h_r} = A \frac{h_\theta}{2}, \quad (4.1)$$

where points  $\mathbf{r}_i$  are shown in Figure 4.1. The parameter  $\Gamma$  is a measure of the curvature-induced mesh deformation relative to  $h_r$ . In a mesh refinement that keeps  $A$  fixed,  $\Gamma = O(Ah_\theta)$  asymptotes to zero. This property implies that on fine enough grids, with fixed curvature and aspect ratio, the impact of curvature on the accuracy of the gradient approximation is diminished.

The following assumptions are made about the grid parameters:  $A \gg 1$ , and  $\Gamma h_r \ll 1$ , which implies that both  $h_r$  and  $h_\theta$  are small,  $h_r \ll Rh_\theta \ll 1$ . For a given aspect ratio,  $A$ , the parameter  $\Gamma$  may vary:  $\Gamma \gg 1$  corresponds to meshes with curvature-induced deformation that is large compared to the radial mesh spacing;  $\Gamma \ll 1$  corresponds to (almost) undeformed meshes.

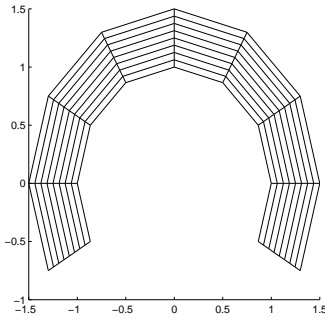
Three types of 2D grids are considered for the cylindrical geometry: (I) *regular quadrilateral grids*; (II) *regular triangular grids* derived from the regular quadrilateral grids by the same diagonal splitting of each quadrangle; (III) *random triangular grids*, in which regular quadrangles are split by randomly chosen diagonals, each diagonal orientation occurring with probability of half. Grids of types (III) are irregular because there is no periodic connectivity pattern. The grid types are shown in Figures 4.2. For a better visualization of the grid topology, low- $\Gamma$  cylindrical grids are shown. Random node perturbation is not applied to high- $\Gamma$  cylindrical grids because even small perturbations in the circumferential direction may lead to non-physical control volumes.

For high- $\Gamma$  grids of these types, one cannot expect a better gradient reconstruction accuracy than the accuracy obtained for grid types (I, II, and III) in rectangular geometry. In this section, we are focusing on difficulties specific to high- $\Gamma$  grids with large curvature-induced deformations. The difficulties arise for functions that are predominantly varying in the radial direction of small mesh spacing. For functions predominantly varying in the direction of small mesh spacing, gradient reconstruction in rectangular geometries is expected to be accurate.

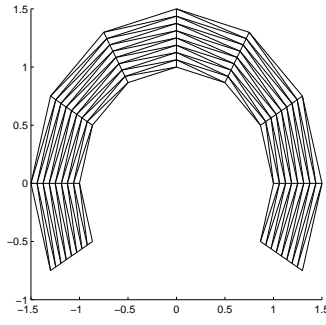
**4.2. Analysis.** To illustrate this new type of difficulty, we analyze least-square C-gradient reconstruction methods for node-centered formulations. Similar analysis has been performed in [11, 12]. Schematic of a stencil is shown in Figure 4.1. Local Cartesian coordinates  $(\xi, \eta)$  are tangential and normal, respectively, to the circumferential grid lines and centered at  $\mathbf{r}_0$ . The nearby points used in the linear least-square fit are denoted with a compass notation. The points are generated from a cylindrical mapping where  $(r, \theta)$  denote polar coordinates with spacings of  $h_r$  and  $h_\theta$ , respectively; the polar coordinates of  $\mathbf{r}_0$  are  $(R, 0)$ .

TABLE 4.1  
Coordinates of points used in linear least-square fit.

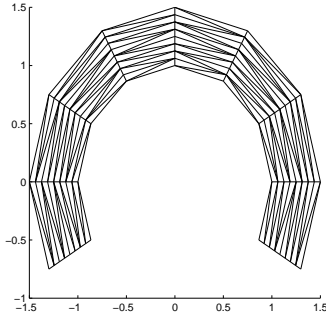
Point	$\xi$	$\eta$	$r$	$\theta$
0	0	0	$R$	0
N	0	$h_r$	$R + h_r$	0
E	$R \sin(h_\theta)$	$-\Gamma h_r$	$R$	$h_\theta$
S	0	$-h_r$	$R - h_r$	0
W	$-R \sin(h_\theta)$	$-\Gamma h_r$	$R$	$h_\theta$



(a) Type (I): Regular quadrilateral grid



(b) Type (II): Regular triangular grid



(c) Type (III): Random triangular grid

FIG. 4.2. Typical cylindrical grids.

A linear least-square fit for a general function  $f(\xi, \eta)$  defined on the dual volume centered at  $\mathbf{r}_0$  can be constructed using the surrounding points  $\mathbf{r}_N, \mathbf{r}_E, \mathbf{r}_S$ , and  $\mathbf{r}_W$  with the coordinates given in Table 4.1. The linear reconstruction,  $f^r(\xi, \eta)$ , of a test function  $f(\mathbf{r})$  is defined as

$$f^r \equiv f_0 + a\xi + b\eta, \quad (4.2)$$

where  $f_0 = f(0, 0)$ . The two parameters  $(a, b)$  are found by minimizing the sum of the squares of the (weighted) differences between  $f(\mathbf{r})$  and the reconstructed values

$$[\mu_N^2(f_N^r - f_N)^2 + \mu_E^2(f_E^r - f_E)^2 + \mu_S^2(f_S^r - f_S)^2 + \mu_W^2(f_W^r - f_W)^2] \rightarrow \min, \quad (4.3)$$

where a subscript denotes a point, e.g.,  $f_E^r = f^r(R \sin(h_\theta), -\Gamma h_r)$ . We can unify description of the CULSQ and CWLSQ methods, assuming  $\mu_N = \mu_S = 1$  and  $\mu_E = \mu_W = \mu$ ;  $\mu = 1$  and  $\mu = \frac{h_r}{2R \sin(\frac{h_\theta}{2})} \approx \frac{h_r}{Rh_\theta}$  for the CULSQ and CWLSQ methods, respectively.

The minimization with  $R = 1$  results in

$$\begin{aligned} a &= \frac{f_E - f_W}{2 \sin(h_\theta)}, \\ b &= \frac{f_N - f_S}{2h_r} - \frac{f_N - f_S}{2h_r} \frac{\mu^2 \Gamma^2}{1 + \mu^2 \Gamma^2} - \frac{f_E - 2f_0 + f_W}{h_\theta^2} \frac{h_\theta^2}{2h_r} \frac{\mu^2 \Gamma}{1 + \mu^2 \Gamma^2}. \end{aligned} \quad (4.4)$$

The leading terms of the gradient approximation,

$$\begin{aligned} a &\approx f_\xi + O(h_\theta^2), \\ b &\approx \frac{f_N - f_S}{2h_r} - \left( \frac{f_N - f_S}{2h_r} + \frac{f_E - 2f_0 + f_W}{h_\theta^2} \right) \frac{\mu^2 \Gamma^2}{1 + \mu^2 \Gamma^2} \\ &= f_\eta - (f_\eta + f_{\xi\xi}) \frac{\mu^2 \Gamma^2}{1 + \mu^2 \Gamma^2} + O\left(h_r^2 + \frac{\mu^2 \Gamma^2 h_\theta^2}{1 + \mu^2 \Gamma^2}\right), \end{aligned} \quad (4.5)$$

indicate that the gradient in the  $\xi$ -direction is always reconstructed with  $O(h_\theta^2)$  accuracy, independent of the least-square weights and/or  $\Gamma$ . The CULSQ method ( $\mu^2 = 1$ ) reconstructs the gradient in the  $\eta$ -direction with the leading error estimated as  $(f_\eta + f_{\xi\xi}) \frac{\Gamma^2}{1 + \Gamma^2}$ . The gradient error in the  $\eta$ -direction is  $O(1)$  on grids with  $\Gamma \gg 1$ , but asymptotically converges with second order in isotropic grid refinement. The CWLSQ method ( $\mu^2 \Gamma^2 = h_\theta^2/4$ ) provides  $O(h_\theta^2)$  accuracy in approximating the  $\eta$ -directional gradient.

To improve the gradient approximation, one can perform a least-square minimization in a mapped domain. Two mapped least-square methods are considered: an exact mapping (CEMLSQ) method that uses the polar coordinates directly; and a more general approximate mapping (CAMLSQ) method that is based on the distance function, defined as the distance to the nearest boundary, normally available in practical schemes. For functions varying predominantly in the direction of small mesh spacing, the least square methods provide accurate gradient reconstruction in rectangular geometries. The CEMLSQ scheme recovers the same accuracy on curved grids of types (I)-(III). Applicability of CEMLSQ is limited to model problems with analytical boundary shape.

The more general CAMLSQ method approximates the CEMLSQ method by applying the least-square minimization in a locally constructed coordinate system.

$$f^r \equiv f_0 + \kappa \xi' + \lambda \eta'. \quad (4.6)$$

The local coordinates,  $(\xi', \eta')$ , are constructed using the distance function, which provides information on the closest boundary point. The coordinate vectors at each point are defined as a unit  $\eta'$ -directional vector pointing in the direction opposite to the closest boundary point and its orthonormal  $\xi'$ -directional vector. The  $\eta'$ -coordinate at each stencil node is its distance from the boundary and the  $\xi'$ -coordinate is the projection of the vector connecting the node with the central node onto the  $\xi'$ -direction. For the cylindrical geometry, the distance function is the shifted radial function,  $r - R$ . Table 4.2 contains CAMLSQ stencil coordinates for geometry shown in Figure 4.1.

In implementation of approximate-mapping method, it is important to have an accurate representation for the distance function. The discrete distance function that provides distances to the flat-panel boundary approximation rather than to the actual boundary may lead to gradient accuracy deterioration. The error introduced into the distance function by the flat-panel boundary approximation is proportional to  $Rh_\theta^2$  and is large comparing to the radial mesh size  $h_r$ . If uncompensated, this error will contribute an  $O(Ah_\theta)$  term into the reconstructed radial gradient. For C-gradient fits on grids of types (I)-(III), this boundary related distance-function error

TABLE 4.2  
Coordinates of points used in CAMLSQ method.

Point	$\xi'$	$\eta'$
0	0	0
N	0	$h_r$
E	$R \sin(h_\theta)$	0
S	0	$-h_r$
W	$-R \sin(h_\theta)$	0

is compensated because it is the same for all points in the stencil. However, for more general grids, e.g., mixed-element grids, an inaccurate distance function degrades accuracy of the approximate-mapping method.

Note that on regular quadrilateral grids, the least-square linear reconstructions in the polar coordinates and in the CAMLSQ local coordinates are fully decoupled; so CEMLSQ and CAMLSQ methods provide second-order accurate approximations  $\kappa = f_r + O(h_r^2)$  and  $\lambda = f_\theta + O(h_\theta^2)$ .

The CAMLSQ method is especially attractive in situations where all other gradient reconstruction methods fail. For example, in some stencils, e.g., the bow-type stencils involving  $\mathbf{r}_0, \mathbf{r}_{NW}, \mathbf{r}_{NE}, \mathbf{r}_{SW}$ , and  $\mathbf{r}_{SE}$ , all peripheral points are (approximately) equidistant from the stencil center, so the CWLSQ method does not help. Mapped least-square methods remain accurate for such stencils.

**4.3. Numerical tests.** Numerical tests are performed on a domain with radial extent of  $[1, 1.000002]$ , angular extent of  $10^\circ$ , and the coarsest grid of  $9 \times 9$  nodes, which leads to high- $\Gamma$  grids with aspect ratio  $A \approx 400,000$  fixed in grid refinement. A radial function,  $U = \sin(100\pi r + \frac{\pi}{8})$ , is the test function. For C-gradients, CULSQ, CWLSQ, and CAMLSQ methods are used in both cell-centered and node-centered formulations. For cell-centered formulations, three types of methods are considered: element-based methods and element-free methods with basic and augmented stencils. Five reconstruction methods for F-gradients in cell-centered formulations are considered: four least square methods (CULSQ, CWLSQ, CEMLSQ, and CAMLSQ) and the NA method. For node-centered formulations, the F-gradients are reconstructed with the GG method. Tables 4.4 and 4.3 summarize the test results concerned with the relative errors of gradient reconstruction. Figure 4.3 illustrates convergence of some C-gradient methods on grids of type (III) for cell-centered formulations.

**4.4. Conclusions.** The results shown in Tables 4.3 and 4.4 lead to the following conclusions.

- The CAMLSQ and FAMLSQ methods provide good accuracy for all gradients on all grids.
- On regular quadrilateral grids of type (I), all methods except the CULSQ method provide good accuracy.
- Node-centered formulations (for C-gradients, in combination with either augmented CWLSQ or CAMLSQ methods) provide accurate gradient reconstruction on all studied grids.
- On triangular grids of types (II) and (III) in cell-centered formulations, the FWLSQ method does not improve over the FULSQ method; both methods exhibit  $O(1)$  error.
- Also on triangular grids of types (II) and (III), both the CULSQ and CWLSQ cell-centered methods exhibit  $O(1)$  error with the basic stencil. Expanding

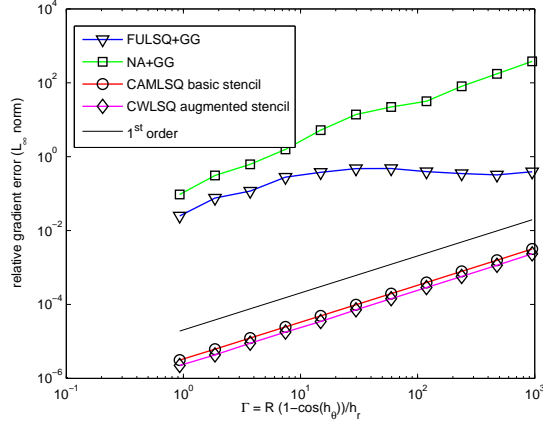


FIG. 4.3. Cell-centered formulation:  $C$ -gradient accuracy for the radial test function on high- $\Gamma$  grids of type (III).

TABLE 4.3  
High- $\Gamma$  grids: relative errors of  $C$ -gradient reconstruction

node-centered formulation			
	(I)	(II)	(III)
CULSQ	$O(1)$	$O(1)$	$O(1)$
CWLSQ	$O(h_\theta^2)$	$O(h_\theta^2)$	$O(h_\theta)$
CAMLSQ	$O(h_\theta^2)$	$O(h_\theta)$	$O(h_\theta)$
cell-centered formulation, basic stencil			
CULSQ	$O(1)$	$O(1)$	$O(1)$
CWLSQ	$O(h_\theta^2)$	$O(1)$	$O(1)$
CAMLSQ	$O(h_\theta^2)$	$O(h_\theta)$	$O(h_\theta)$
cell-centered formulation, augmented stencil			
CULSQ	$O(1)$	$O(1)$	$O(1)$
CWLSQ	$O(h_\theta^2)$	$O(h_\theta^2)$	$O(h_\theta)$
CAMLSQ	$O(h_\theta^2)$	$O(h_\theta)$	$O(h_\theta)$
cell-centered formulation, element-based			
NA+GG	$O(h_\theta^2)$	$O(h_\theta)$	$O(Ah_\theta)$
FULSQ+GG	$O(h_\theta^2)$	$O(h_\theta)$	$O(1)$
FWLSQ+GG	$O(h_\theta^2)$	$O(h_\theta)$	$O(1)$

the least-square stencil beyond immediate neighbors (augmentation) does not provide accuracy benefits for the CULSQ method, but is beneficial for the CWLSQ method.

- In cell-centered formulations, the element-based methods provide  $C$ -gradient benefits only over the CULSQ method on grids of type (I) and (II). On grids of type (III), the error of the NA+GG method is  $O(Ah_\theta)$ .
- The NA method provides accurate  $F$ -gradient approximations for regular grids, but exhibits  $O(Ah_\theta)$  relative errors for gradients on high- $\Gamma$  grids of type (III); these large errors occur at the radial faces.

TABLE 4.4  
*High- $\Gamma$  grids: relative errors of  $F$ -gradient reconstruction*

node-centered formulation			
	(I)	(II)	(III)
Green-Gauss	$O(h_\theta^2)$	$O(h_\theta)$	$O(h_\theta)$
cell-centered formulation			
FULSQ	$O(h_\theta^2)$	$O(1)$	$O(1)$
FWLSQ	$O(h_\theta^2)$	$O(1)$	$O(1)$
FEMLSQ	$O(h_r^2)$	$O(h_r^2)$	$O(h_r^2)$
FAMLSQ	$O(h_\theta^2)$	$O(h_\theta^2)$	$O(h_\theta^2)$
NA	$O(h_\theta^2)$	$O(h_\theta^2)$	$O(Ah_\theta)$

**5. Additional remarks.** The study is intended to be a reference guide accompanying the construction of accurate and efficient FVD methods for high Reynolds number flow applications. It is focused on gradient reconstruction accuracy; other related issues, such as solution accuracy and stability, have not been considered. Nevertheless, we remark on several issues that are important in this context of constructing flow solvers.

*Remark 1.* A poor gradient reconstruction accuracy does not necessarily imply large discretization error. For example, some discretizations based on CULSQ method are known to produce (second-order) accurate solutions [11] even on grids where the CULSQ method has a large gradient reconstruction error. This counterintuitive observation is explained by the fact that the large  $O(Ah_x)$  error affects the gradient in the  $y$ -direction of small mesh spacing on grids where  $h_y \ll h_x^2$ . The solution reconstruction error introduced by the gradient inaccuracy on such grids is second-order small  $O(Ah_x h_y) = O(h_x^2)$ .

*Remark 2.* In practical computations, high-aspect ratio grids are generated to better approximate certain components of the solutions, e.g., velocity components in viscous boundary layers. These grids are typically well suited to provide accurate gradients for the target solution components; however, gradients of other solution components, e.g., pressure, computed on these grids might be inaccurate. This limitation should be considered in constructing limiters that rely on ratios of gradients.

*Remark 3.* For node-centered formulations, the CWLSQ method provides accurate C-gradient approximations. However, serious convergence difficulties have been reported ([15]) using defect-correction iterations with the CWLSQ method.

*Remark 4.* Additional difficulty associated with the NA schemes [6] stems from the fact that, for stability, the coefficients of the pseudo-Laplacian used in the averaging are clipped between 0 and 2. This clipping can lead to significant inaccuracies in gradient reconstruction.

**6. Conclusions.** The accuracy of the gradient approximation is a key contributor to solution accuracy. A comprehensive and systematic evaluation of the accuracy of gradients needed in unstructured-grid finite-volume schemes intended for high Reynolds number applications has been presented. The accuracy and asymptotic order properties of within-cell and within-face gradient approximations have been shown for current algorithms used in both node-centered and cell-centered formulations. The evaluations have been made for high-aspect-ratio grids in both Cartesian and cylindrical geometries using six grid topologies with quadrilateral, triangular, and mixed element types, with and without random perturbations. The study shows that the

accuracy of gradient reconstruction at high aspect-ratio is determined by a combination of grid and solution. On general unstructured meshes with aspect ratios high enough, so that the product of the aspect ratio and the bigger mesh spacing is much larger than one, any conventional gradient reconstruction method produces large errors for gradients of well-resolved and smooth solutions that vary predominantly in the direction of big mesh spacing, e.g., pressure in a boundary-layer type mesh. Specific comparisons of the relative differences between node-centered and cell-centered approaches using Green-Gauss, unweighted and weighted least-squares, and node-averaging methods have been given. The study is intended to be a reference guide accompanying the construction of accurate and efficient methods for high Reynolds number flow applications.

Specific approaches to reduce errors encountered in applications are given. One approach is to monitor the terms in the solution contributing to the error and add higher-order terms in the direction of larger mesh spacing. Another approach is to employ an approximate-mapped least-square method based on the distance function that is normally available in practical schemes. In curved geometries, the latter approach provides accurate gradient reconstruction on general high-aspect-ratio grids.

#### REFERENCES

- [1] W. K. ANDERSON AND D. L. BONHAUS, *An implicit upwind algorithm for computing turbulent flows on unstructured grids*, Computers and Fluids, 23 (1994), pp. 1–21.
- [2] I. BABUSHKA AND A. K. AZIZ, *On the angle condition in the finite element method*, SIAM J. Numer. Anal., 13 (1976), pp. 214–226.
- [3] T. J. BARTH, *Numerical aspects of computing high-Reynolds number flow on unstructured meshes*, AIAA Paper 91-0721, 29-th AIAA Aerospace Science Meeting, Reno, NV, January 1991.
- [4] M. BERZINS, *A solution-based triangular and tetrahedral mesh quality indicator*, SIAM J. Sci. Comput., 19 (1998), pp. 2051–2060.
- [5] J. BLAZEK, *Computational Fluid Dynamics: Principles and Applications*, Elsevier, 2001.
- [6] N. T. FRINK, *Assesment of an unstructured-grid method for predicting 3-D turbulent viscous flows*, AIAA Paper 96-0292, 34-nd AIAA Aerospace Science Meeting and Exhibit, Reno, NV, January 1996.
- [7] A. C. HASELBACHER, *On constrained reconstruction operators*, AIAA Paper 2006-1274, 44-th AIAA Aerospace Science Meeting and Exhibit, Reno, NV, January 2006.
- [8] A. C. HASELBACHER, J. J. MCGUIRK, AND G. J. PAGE, *Finite-volume discretization aspects for viscous flows on mixed unstructured grids*, AIAA Journal, 37 (1999), p. 477.
- [9] D. G. HOLMES AND S. D. CONNELL, *Solution of the 2D Navier-Stokes equations on unstructured adaptive grids*, AIAA Paper 89-1392, 9-th AIAA CFD conference, Washington, DC, June 1989.
- [10] M. KRIZEK, *On the maximum angle condition for linear tetrahedral elements*, SIAM J. Numer. Anal., 29 (1992), pp. 513–520.
- [11] D. J. MAVRIPLIS, *Revisiting the least-square procedure for gradient reconstruction on unstructured meshes*, AIAA Paper 2003-3986, 18-th AIAA CFD conference, Orlando, FL, June 2003.
- [12] N. V. PETROVSKAYA, *The choice of weight coefficients for least-square gradient approximation*, J. Math. Mod., 16(5) (2004), pp. 83–93. (in Russian).
- [13] R. D. RAUSCH, J. T. BATINA, AND H. T. YANG, *Spatial adaptation procedures on unstructured meshes for accurate unsteady aerodynamic flow computation*, AIAA Paper 89-1392, 9-th AIAA CFD conference, Washington, DC, June 1989.
- [14] S. RIPPA, *Long and thin triangles can be good for linear interpolation*, SIAM J. Numer. Anal., 29 (1992), pp. 257–270.
- [15] T. M. SMITH, M. F. BARONE, R. B. BOND, A. A. LORBER, AND D. G. BAUR, *Comparison of reconstruction techniques for unstructured mesh vertex centered finite volume scheme*, tech. rep., 18-th AIAA CFD Conference, Miami, FL, June 2007. AIAA Paper 2007-3958.
- [16] G. STRANG AND G. J. FIX, *An Analysis of the Finite Element Method*, Prentice-Hall, USA, 1973.